Spin-torque oscillator using a perpendicular polarizer and a planar free layer

D. HOUSSAMEDDINE[1]*, U. EBELS[1]*†, B. DELAËT[2]*, B. RODMACQ[1], I. FIRASTRAU[1,2,3], F. PONTHENIER[2], M. BRUNET[2]‡, C. THIRION[1], J.-P. MICHEL[2], L. PREJBEANU-BUDA[1], M.-C. CYRILLE[2], O. REDON[2] AND B. DIENY[1]

[1]SPINTEC URA 2512, C.E.A/DRFMC - C.N.R.S, CEA-Grenoble, 17 rue des Martyrs, 38054 Grenoble, France
[2]LIMN/DIHS/LETI CEA-Grenoble, 17 rue des Martyrs, 38054 Grenoble, France
[3]Transilvania University of Brasov, 29 Bulevardul Eroilor, R-500036 Brasov, Romania
*These authors contributed equally to this work
‡Present address: LAAS - CNRS, 7 av du colonel Roche, 31077 Toulouse Cedex 4, France
†e-mail: ursula.ebels@cea.fr

Published online: 29 April 2007; corrected online 8 May 2007 (details online); doi:10.1038/nmat1905

Spintronics materials have recently been considered for radio-frequency devices such as oscillators by exploiting the transfer of spin angular momentum between a spin-polarized electrical current and the magnetic nanostructure it passes through. While previous spin-transfer oscillators (STOs) were based on in-plane magnetized structures, here we present the realization of an STO that contains a perpendicular spin current polarizer combined with an in-plane magnetized free layer. This device is characterized by high-frequency oscillations of the free-layer magnetization, consistent with out-of-plane steady-state precessions induced at the threshold current by a spin-transfer torque from perpendicularly polarized electrons. The results are summarized in static and dynamic current–field state diagrams and will be of importance for the design of STOs with enhanced output signals.

The possibility to excite large-angle steady-state precessions of the free-layer magnetization in spin valves or magnetic tunnel junctions, using a spin-polarized d.c. current[1–4], has recently attracted much attention[5–15]. In combination with the magnetoresistance (MR)[16,17] of such devices (see Fig. 1), these magnetization oscillations open the way for new applications of spin-electronics materials in the area of radio-frequency (RF) devices. One example will be wide-band tuneable RF oscillators[18]. From a more fundamental point of view, the spin-polarized current-induced precessions provide the possibility to study new nonlinear dynamic effects of the magnetization for individual[19–21] or coupled[11–14,22] oscillators.

In a single-spin (or macrospin) description, the spin-polarized current-induced steady-state precessions correspond to lossless constant-energy trajectories[4,23–25], for which the spin-transfer torque opposes and cancels on average the damping ('loss') torque. The remaining precession torque induces a periodic gyromagnetic motion of the magnetization in response to the internal effective fields[4,23–25]. Whereas the character of the constant-energy trajectories is determined by the underlying system energy, the selection of a particular trajectory and energy level depends on the spin-polarization direction and the current amplitude $I_{d.c.}$ (given that $I_{d.c.}$ is larger than a critical (or threshold) current I_c).

For the case of interest here, which is a thin-film magnetic element with uniaxial in-plane anisotropy and under in-plane bias fields, two classes of magnetization trajectories can be distinguished[4,5,23,24]. They are commonly called in-plane (IP) precession, characterized by an oscillation around the static IP energy minimum, and out-of-plane (OP) precession, characterized by an oscillation around the OP energy maximum, as illustrated in Fig. 1b. The properties of these trajectories differ in many ways. One parameter relevant for applications is the output signal ΔU, which is proportional to the dynamic resistance variation ΔR_{IP} or ΔR_{OP}. As indicated in Fig. 1b, ΔR_{IP} and ΔR_{OP} are given by the maximum excursions of the free-layer magnetization during the precessional motion on IP or OP trajectories. The upper limit for the dynamic resistance variation is the static variation ΔR_{stat}, which is defined by the difference in resistance between the parallel and antiparallel alignments of the free-layer magnetization with respect to an analysing layer. As shown in Fig. 1b, larger output signals are expected for OP trajectories, where the magnetization oscillates almost between the P and AP states.

Experimentally, it has been shown that OP trajectories can be induced in 'planar' spin-valve structures, where both the free layer and the polarizing layer are IP magnetized. This requires either relatively large current amplitudes[4,5,7] or relatively large OP bias fields[6], which is not suitable for RF applications. In contrast, here experimental evidence is provided for OP precessions that are induced close to the critical current I_c as well as in zero external field. This is achieved by choosing an OP magnetized polarizer combined with an IP magnetized free layer, as theoretically described in refs 18,26–28. This configuration differs from that reported recently[29], where both the polarizer and the free layer are OP magnetized.

Before addressing the experimental results, we will first summarize macrospin simulations that describe the action of perpendicularly polarized electrons on an IP magnetized free layer with uniaxial IP anisotropy[27,30]. A calculated current–field state

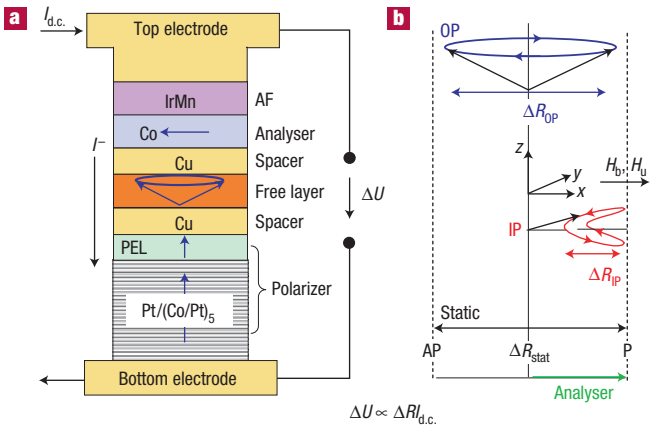

Figure 1 Magneto-resistive cell and magneto-resistance. a, Schematic diagram of a magneto-resistive cell consisting of a perpendicular polarizer, a free layer and an analyser coupled to an antiferromagnet (AF). PEL means polarization enhancement layer. The role of the polarizer is to spin polarize the conduction electrons on passing a d.c. current $I_{d.c.}$ through the stack. The precession of the free-layer magnetization creates an a.c. output voltage ΔU, proportional to the dynamic MR variation ΔR. **b**, Schematic diagram of the IP and OP precession trajectories with their respective dynamic resistance variations ΔR_{IP} and ΔR_{OP}. ΔR_{stat} is the static resistance variation between the parallel (P) and antiparallel (AP) alignments of the free layer with respect to the analyser magnetization. H_u is the uniaxial anisotropy field and the corresponding easy axis is the *x* axis. The bias field H_b is applied parallel to the easy axis.

diagram is given in Fig. 2a, showing the critical current I_c as a function of an IP bias field H_b, applied parallel to the easy axis. In the region denoted pseudo-P (AP) in the diagram of Fig. 2a (white region for $I_{d.c.} < I_c(H_b)$), the spin torque balances the precession torque, whose strength is determined by the anisotropy field H_u and the bias field H_b. This results in a static equilibrium, where the magnetization is rotated away from the initial P or AP state. When the current is larger than the critical current, $I_{d.c.} \geq I_c(H_b)$, this static equilibrium becomes unstable and the magnetization goes into OP oscillations (orange areas in Fig. 2a). The critical current $I_c(H_b)$ in Fig. 2a delineates two triangular shaped regions of OP precession that are symmetrical with respect to zero current and zero bias field[30]. The linear increase of I_c is approximately proportional to $(0.5H_u \pm H_b)/g$, where g is the spin-polarization efficiency[1]. Since the spin-polarized current pushes the magnetization out of plane, the OP precession trajectory can be characterized by its OP magnetization component M_z, which is smallest at the threshold current and then increases proportionally to $I_{d.c.}$. The associated demagnetization field determines the precession frequency, with $f \propto M_z$, which therefore increases linearly on increasing current $I_{d.c.}$ (ref. 27); see Fig. 2b. In contrast to this increase, the frequencies as a function of an IP bias field decrease in a parabolic way[23] (see Fig. 2c), as H_b pulls the magnetization back into the plane, thus decreasing the average OP magnetization component M_z.

It is emphasized that both the symmetric state diagram and the current and field dependencies of the described OP precession frequencies are quite different from IP precessions that are induced by IP-polarized electrons[4,5]. In the latter case, IP precessions are excited at the threshold current in regions that are asymmetric with respect to the current–field axes[5,24,31–33]. Their corresponding frequencies decrease with increasing current and increase with field[4,5,23,24]. The state diagram and the frequency dependence therefore provide a means to determine the character of precession modes as well as the associated spin-polarization direction (IP versus perpendicular).

Up to now, the current–field state diagram as well as the associated dynamics have not been verified experimentally for this 'perpendicular-polarizer/planar-free-layer' geometry. This is because of two major difficulties. First, from a materials point of view, we have to choose a polarizer that combines a large OP anisotropy with a sufficiently large spin polarization[29]. Second, as the M_z component varies little along an OP trajectory, the dynamic MR variation between the polarizer and the free layer is very small. In consequence, a third IP-magnetized analysing spin valve or tunnel-junction system is required on top of the free layer to monitor the free-layer magnetization motion[18,26–28]. However, care has to be taken that the spin-transfer torque from the perpendicular polarizer dominates over that from the planar analyser. This can be achieved by using materials of different spin polarizations and/or spin diffusion lengths. A first realization of this 'perpendicular-polarizer/planar-free-layer/planar-analyser' configuration has been reported in ref. 34, where the static reversal was addressed. It was observed that the critical current for reversal, induced by the planar analyser, is reduced in the presence of a perpendicular polarizer.

In order to design a polarizer that combines an OP magnetization with a strong spin polarization, here we have used a Pt/(Co/Pt)$_5$ multilayer structure with strong OP anisotropy, induced at the Co/Pt interfaces. The presence of Pt however does not allow us to construct a sufficient spin polarization owing to strong spin–orbit scattering inside the Pt layers. Therefore, a polarization-enhancement layer (PEL) composed of a thin Co layer laminated with one thin Cu interlayer[35,36] was deposited on top of the Co/Pt multilayer structure. Its thickness is of the order of its effective spin diffusion length. The final composition of our spin-transfer oscillator is as follows: Pol/Cu/FeNi/Co/Cu/Co/IrMn. Here, Pol corresponds to Pt/(Co/Pt)$_5$/(Co/Cu/Co) and the bilayer FeNi/Co constitutes the planar free layer. The Co in the bilayer Co/IrMn corresponds to the planar analysing layer coupled to an IrMn antiferromagnet to pin its magnetization direction. In order to reduce the spin-polarization effects from the planar analyser, its thickness has been chosen to be one-tenth of the corresponding spin diffusion length.

Static and dynamic transport measurements were made for nanopillar devices as a function of an IP bias field H_b, monitoring the MR of the planar spin-valve substructure of FeNi/Co/Cu/Co/IrMn. The influence of the perpendicular polarizer on the free-layer magnetization and thus on the planar MR was then studied as a function of the current amplitude. While similar results have been obtained on a variety of samples, measurements will be presented here only for one particular sample of elliptical shape with nominal dimensions of $60 \times 70\,nm^2$.

A typical MR transfer curve as a function of H_b and for low bias current $I_{d.c.} = -0.15\,mA$ is shown in Fig. 3, revealing a static MR variation of $\Delta R_{stat} = 0.19\,\Omega$ and an MR ratio of 0.33%. The low MR ratio is due to the large series resistance arising from contact electrodes inside the nanopillar. The loop in positive H_b is identified as the reversal of the analysing layer (Au), whereas the loop in negative H_b is identified as the free-layer reversal (FL). Its shift to $H_b = -26.3\,kA\,m^{-1}$ is due to dipolar stray fields from the analysing layer. The external field that the free layer is seeing is therefore the effective bias field H_{beff}, defined here by $H_{beff} = H_b + 26.3\,kA\,m^{-1}$, with H_b the applied bias field. All subsequent experimental data will be consequently plotted versus H_{beff}. It is noted that this offset can be eliminated by choosing a compensated synthetic antiferromagnet for the analyser. Last, in our experiments, negative current corresponds to electrons flowing from the polarizing layer to the free layer (see Fig. 1a). The maximum excursions in current

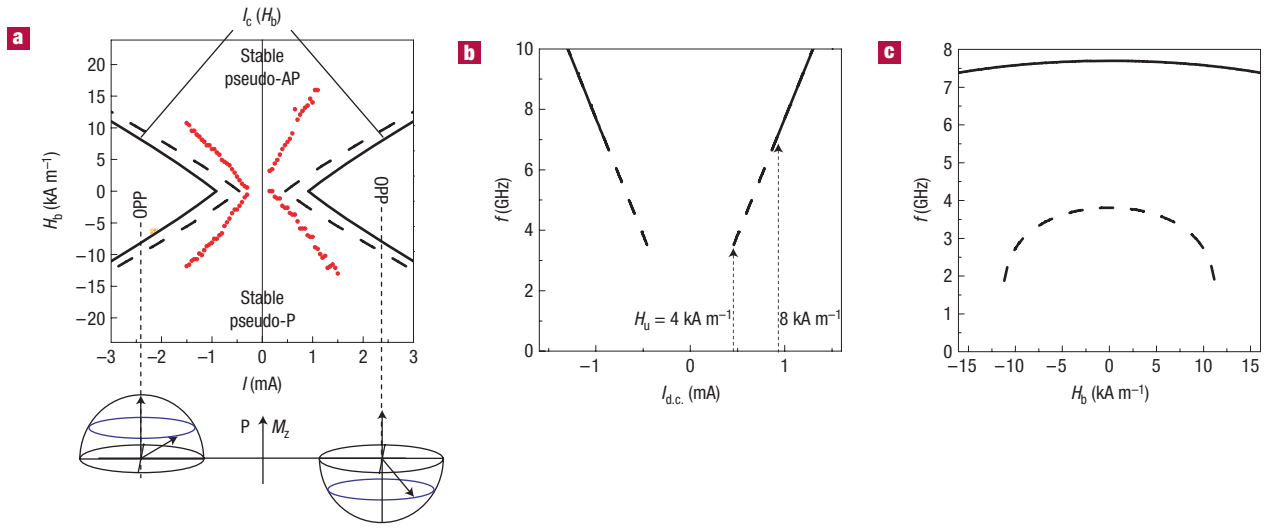

Figure 2 Macrospin simulations. a, Calculated state diagram with critical boundaries $I_c(H_b)$ versus IP bias field H_b. Boundaries are shown for two values of the uniaxial anisotropy field $H_u = 8\,\mathrm{kA\,m^{-1}}$ (full line) and $H_u = 4\,\mathrm{kA\,m^{-1}}$ (dashed line). OPP denotes the region of steady-state out-of-plane precession (orange region for $H_u = 8\,\mathrm{kA\,m^{-1}}$). The red circles are the experimental boundaries of Fig. 4c, for which H_b corresponds here to the effective bias field H_{beff}. Bottom: schematic diagrams of the OP precession trajectories (blue) on the unit sphere. **b**, Linear increase of the frequency versus current $I_{d.c.}$ for two values of H_u and for zero bias field. While the slope $df/d|I_{d.c.}|$ is the same, the critical current and with this the minimum frequency is lower for smaller H_u, as indicated by the dashed arrows. **c**, Frequency versus bias field close to the critical current with $I_{d.c.} = 0.5\,\mathrm{mA}$ ($H_u = 4\,\mathrm{kA\,m^{-1}}$, bottom) and 1 mA ($H_u = 8\,\mathrm{kA\,m^{-1}}$, top). The parabolic behaviour is similar to ref. 23, where oscillations close to the OP maximum are described. The parameters of the simulation are given in the Methods section.

were limited to $I_{d.c.} = \pm 1.5\,\mathrm{mA}$ (corresponding current density $J = -4.5 \times 10^7\,\mathrm{A\,cm^{-2}}$) so as not to heat the sample and cause irreversible damage.

Figure 4a shows the evolution of the free-layer minor loop $R(H_{beff})$ for different current amplitudes. At low current ($\pm 0.1\,\mathrm{mA}$), the reversal between the AP and P state occurs in a single step. The corresponding coercivity of $0.8\,\mathrm{kA\,m^{-1}}$ is much lower than the shape anisotropy field H_u, which is estimated to be $8\,\mathrm{kA\,m^{-1}}$. The reversal at low current is thus probably not a coherent reversal process and also strongly thermally activated. On increasing $I_{d.c.}$ from zero to negative values in Fig. 4a, a plateau at an intermediate resistance level (IRL) starts to become apparent at $I_{d.c.} = -0.3\,\mathrm{mA}$. Its width increases with increasing current amplitude and its associated resistance change is roughly one-half of the full MR variation ΔR_{stat}. The same plateau is obtained for positive currents above $I_{d.c.} = 0.15\,\mathrm{mA}$. A detailed $R(H_{beff})$ minor loop is shown in Fig. 4b (top) for $I_{d.c.} = 0.7\,\mathrm{mA}$. It is noted that in the $R(H_{beff})$ loops the full MR amplitude of $\Delta R_{stat} = 0.19\,\Omega$ is maintained when sweeping between the maximum and minimum bias field values of Fig. 4a. This indicates that the associated minimum and maximum resistance values correspond respectively to the P and AP configurations. Similar steps from the AP or P states to an IRL can be observed in resistance versus current, $R(I_{d.c.})$, loops taken at different H_{beff} values, as shown in Fig. 4b (bottom). Here, the resistance around zero current corresponds to an AP high-resistance (P low-resistance) state when $H_{beff} > 0$ (< 0). For increasing current amplitude the resistance drops (increases) towards the IRL.

The critical currents $I_c(H_{beff})$ where the steps towards the IRL occur are summarized in a static current–field state diagram in Fig. 4c. They delineate two triangular-shaped regions centred on zero current and zero field, similar to Fig. 2a. The squares correspond to the values deduced from $R(H_{beff})$ loops and the circles to those deduced from $R(I_{d.c.})$ loops (see Fig. 4b). There is good agreement for the boundaries $I_c(H_{beff})$ deduced from either

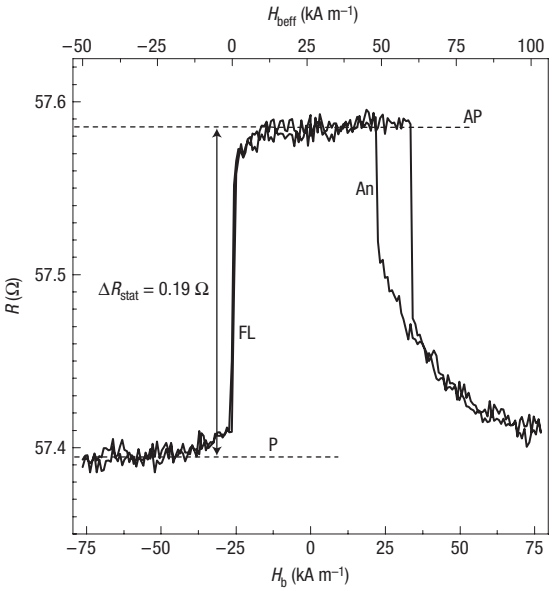

Figure 3 Magneto-resistive transfer curve. Resistance versus IP bias field H_b for the 'perpendicular-polarizer/planar-free-layer/planar-analyser' spin-valve structure described in the text. The top scale shows the effective bias H_{beff} of the free layer, shifted by $26.3\,\mathrm{kA\,m^{-1}}$ with respect to the applied bias field H_b.

set of loops, except at positive $I_{d.c.}$ and positive H_{beff}, where the IRL region is broadened. In this part of the diagram an additional boundary exists, which corresponds to a shoulder in the $R(H_{beff})$ loops for the transition from the IRL to the AP state at $I_{d.c.} > 0$. This shoulder can be seen in detail in Fig. 4b (top), where this

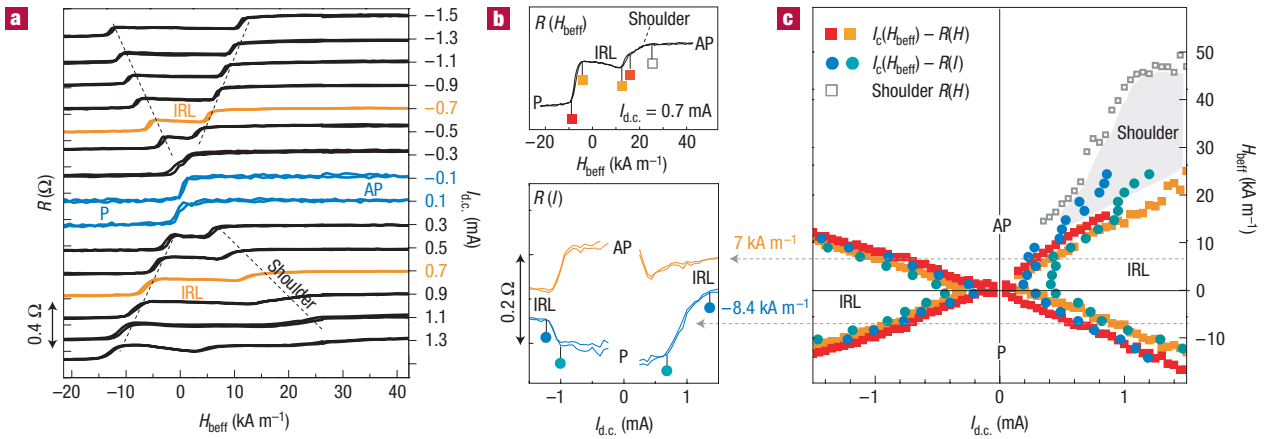

Figure 4 Hysteresis loops and static state diagram. a, Minor loops $R(H_{beff})$ of the resistance versus effective IP bias field H_{beff} for different currents $I_{d.c.}$ of −1.5 to 1.3 mA, in increments of 0.2 mA. The resistance loops are offset for clarity. The dashed lines are guides for the eye to indicate the transition to the intermediate resistance level (IRL). **b**, Top: Detailed $R(H_{beff})$ loop for $I_{d.c.} = 0.7$ mA. Bottom: $R(I)$ loops for $H_{beff} = +7$ kA m^{-1} (orange line) and -8.4 kA m^{-1} (blue line). The red and orange squares as well as the green and blue circles indicate the reading of the critical current $I_c(H_{beff})$. **c**, Static state diagram $I_{d.c.}$–H_{beff} for the IRL (orange region) and the shoulder region deduced from the $R(H_{beff})$ (squares) and $R(I)$ (circles) loops.

transition is much less abrupt and stretches over a relatively large field range.

In the following we will focus on the IRL. The similarity of the corresponding experimental state diagram in Fig. 4c to the predicted one shown in Fig. 2a leads to the suggestion that the IRL is due to OP oscillations in the free layer, induced by the spin-transfer torque from perpendicularly polarized electrons. Considering, furthermore, that in the static experiments the resistance is averaged over the OP precession trajectories, this identification is then consistent with the resistance change of the IRL being roughly one-half of the full MR change ΔR_{stat}.

The identification of the IRL with OP steady-state precessions is confirmed by dynamic magneto-transport experiments. Typical (gain-corrected) spectra for the power spectral density of the output voltage ΔU are shown for negative and positive current in Fig. 5a ($H_{beff} = 0.72$ kA m^{-1}). High-frequency oscillations start to become apparent above the noise at $I_{d.c.} = \pm 0.3$ mA with frequencies ranging from 2 to 4 GHz. For both positive and negative current, the corresponding frequencies first increase relatively steeply with increasing current up to approximately 1 mA and then decrease slightly; see Fig. 5c. The initial increase is denoted by mode f1 and the decrease by mode f2. The appearance of both modes as a function of $I_{d.c.}$ and H_{beff} is summarized in the dynamic state diagram in Fig. 5d, which is superposed onto the static diagram. There is exact correspondence between the static critical lines $I_c(H_{beff})$ and the appearance of the dynamic modes f1 and f2. However, no systematic dependence is apparent for the transition between modes f1 and f2, only a specific asymmetry with respect to the sign of the current, with a larger region of mode f1 for positive current.

The positive slope $df/d|I_{d.c.}|$ of mode f1 (Fig. 5c) is qualitatively in agreement with macrospin simulations shown in Fig. 2b. Also in qualitative agreement is the parabolic dependence of f1 on the effective bias field[23], with f decreasing on increasing H_{beff} for both negative and positive values. This is shown in Fig. 5b for $I_{d.c.} = 0.8$ mA, where the frequency dependence of f1 is given together with the static $R(H_{beff})$ hysteresis loop. Mode f1 appears only in the plateau region of the IRL. In contrast to this, the slight decrease in frequency versus $|I_{d.c.}|$ of mode f2 above ±1 mA is not explained by macrospin simulations. Furthermore, this decrease seems to be associated with an upward (downward) jump in frequency for negative (positive) current that can be clearly seen in the spectra of Fig. 5a for $I_{d.c.} < 0$. We have denoted this branch by mode f2 as it is not a priori clear whether it is of the same nature as mode f1. However, as shown in Fig. 5b for $I_{d.c.} = -1.3$ mA, the corresponding effective bias field dependence is the same as for mode f1. This dependence as well as its occurrence only in the region of the IRL indicates that mode f2 is also an OP oscillation.

While there is a good qualitative agreement of the behaviour of mode f1 with the macrospin predictions of OP oscillations induced by perpendicularly polarized electrons, we would like to comment on the quantitative differences of the values of the frequencies (see Figs 2b and 5c) as well as on the negative slope of mode f2. The frequency is determined by the OP magnetization component M_z, which is given by the balance between the spin-transfer torque that pushes the magnetization OP and the damping torque that pulls the magnetization back to its equilibrium IP. In the macrospin description, the slope $df/d|I_{d.c.}|$ is therefore proportional to the ratio between the spin-polarization efficiency g and the damping constant α (ref. 27), $df/d|I_{d.c.}| \propto g/\alpha$. The experimental slopes of mode f1 in Fig. 5c are smaller by a factor of two to three than that of the simulated frequencies in Fig. 2b. This indicates that in the experiment the actual spin-polarization efficiency g might be smaller and/or the damping constant larger than the values used in the simulation ($g = 0.17$ and $\alpha = 0.02$). However, other factors will contribute to the reduced experimental frequency values as well. One of them is most likely related to the fact that the critical current $I_c(H_{beff})$ is lower in the experiment than in the simulations; see Fig. 2a. A possible origin for this difference is the actual value of the anisotropy field H_u. For example, small deviations of only ±2 nm of the ellipse axes (62 nm × 68 nm) result in a shape-anisotropy field of 4.8 kA m^{-1}, which is almost one-half of that for the nominal size of 60 nm × 70 nm. As shown in Fig. 2a,b, a reduction in H_u leads to a lower critical current and with this to lower frequencies. Other factors that will contribute to the reduced values of I_c and f are thermal activation as well as the true micromagnetic configuration. The finite size of the elliptical element, as well as the dipolar stray fields from the polarizer and analyser, will result in a non-homogeneous (non-macrospin) magnetization distribution. An indication for the importance of this non-homogeneous

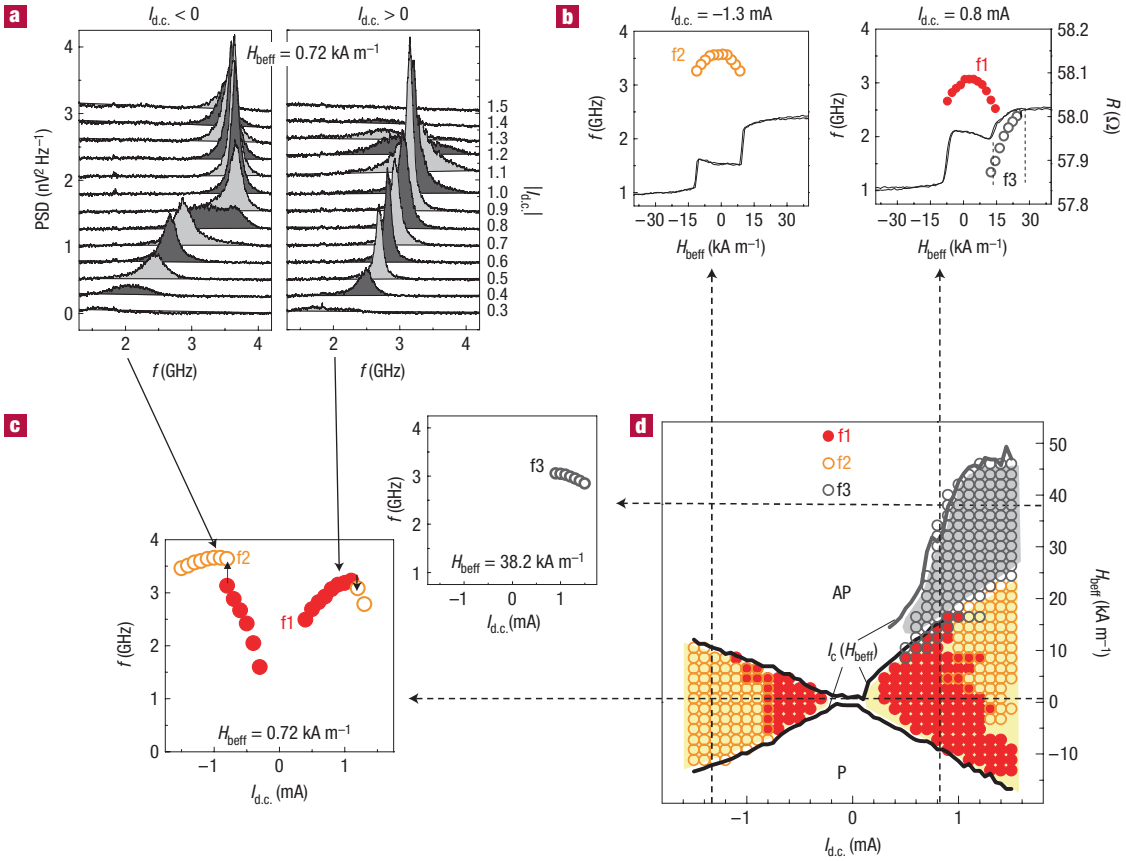

Figure 5 Dynamic spectra and dynamic state diagram. a, Power spectral density (PSD) of the output voltage ΔU (see Fig. 1) obtained in the IRL region for $H_{beff} = 0.72$ kA m^{-1} at positive and negative $I_{d.c.}$. The current amplitudes range from 0.3 to 1.5 mA in increments of 0.1 mA. The spectra are offset for clarity. **b**, Frequency versus H_{beff} for mode f2 at $I = -1.3$ mA (left) and modes f1 and f3 at $I = 0.8$ mA (right) superposed onto the corresponding $R(H_{beff})$ loops. **c**, Frequency versus $I_{d.c.}$ of modes f1 and f2 for $H_{beff} = 0.72$ kA m^{-1} Oe (left) and of mode f3 for $H_{beff} = 38.2$ kA m^{-1} (right). **d**, Dynamic state diagram for modes f1 (red filled circles), f2 (orange open circles) and f3 (grey open circles), superposed onto the static state diagram with boundaries $I_c(H_{beff})$ (black lines) for the IRL (yellow background) and the shoulder region (grey background).

configuration is the decrease in frequency for mode f2, which has qualitatively been reproduced by preliminary micromagnetic simulations (not shown here). These simulations reveal that above a certain current value the system creates small vortex-like regions with a relatively strong M_z component and larger regions with a relatively small M_z component. The reduced average M_z value minimizes the demagnetization field energy and results in a reduced frequency on increasing current. These simulations suggest that mode f2 is essentially the same as mode f1, whose frequency changes owing to changes in the magnetization configuration.

We would like to indicate that the change of slope for mode f2 is not considered to be due to a spin-polarization effect from the planar analyser, as might be suggested, as all simulations above have ignored this effect. Macrospin simulations, though taking both the perpendicular polarizer and the planar analyser into account, do not indicate any such change of the slope $df/d|I_{d.c.}|$, which is always positive. This however does not mean that the effect of the analyser is absent. For example, we attribute the presence of the additional region labelled by 'shoulder' in the static diagram of Fig. 4c to the analyser. In this shoulder region, dynamic excitations have been observed that are denoted mode f3 in Fig. 5b–d. Their corresponding frequencies decrease with increasing current (Fig. 5c) and increase with effective bias field (Fig. 5b). This is the signature of an IP steady-state precession[4,5,24] that we attribute to excitations of the free-layer magnetization in the AP state induced by IP-polarized electrons. These IP oscillations explain the reduction of the resistance of the shoulder below the resistance of the AP state; see Fig. 4b top and Fig. 5b right. Let us point out that these IP precessions are present only outside the IRL, which means that the planar analyser does not modify the character of the OP oscillations in a substantial way. Its influence is rather seen in the various asymmetries that can be noted in Figs 4 and 5 for modes f1 and f2 with respect to the sign of the current.

As a final point, it will be of interest to compare the precession amplitudes and generated voltage signals for IP and OP oscillations. As has been mentioned in the introduction, larger precession amplitudes and thus a larger output voltage are expected for OP precession as compared with IP at the threshold current. We have therefore extracted the dynamic resistance variations ΔR_{IP} for IP and ΔR_{OP} for OP oscillations, which are defined in Fig. 1b. These resistance variations have been deduced from the measured power spectral densities and are plotted in Fig. 6 as a function of current. ΔR_{OP} is largest for mode f1 ($H_{beff} = 0.72$ kA m^{-1}) at the threshold current ($I_c = \pm 0.3$ mA) and decreases continuously for modes f1 and f2 with increasing current amplitude. This is consistent with OP precessions induced by the perpendicular polarizer, for which

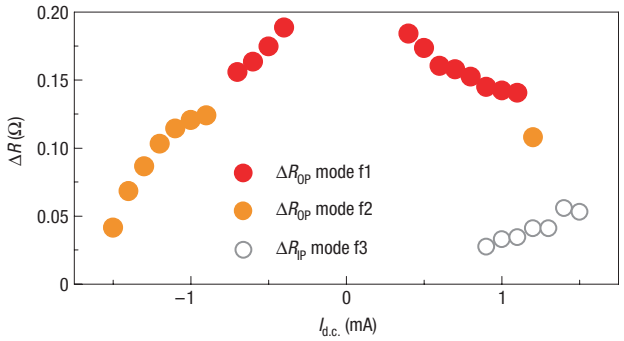

Figure 6 Dynamic resistance variation. ΔR_{OP} for modes f1 (red) and f2 (orange) at $H_{beff} = 0.72\,kA\,m^{-1}$ and ΔR_{IP} for mode f3 (grey open circles) at $H_{beff} = 38.2\,kA\,m^{-1}$.

M_z increases continuously on increasing current. As a consequence, the IP projection of the free-layer magnetization, which determines ΔR_{OP}, decreases; compare Figs 1b and 2a bottom. In contrast, ΔR_{IP} for mode f3 ($H_{beff} = 38.2\,kA\,m^{-1}$) is smallest at the threshold current ($I_c = 0.9\,mA$) and increases with current, consistent with an increase of the IP precession amplitude induced by IP-polarized electrons[4,5,24]. From Fig. 6 it can be confirmed that ΔR_{OP} is indeed larger than ΔR_{IP}. Considering the associated peak-to-peak voltage $\Delta U_{gen} = \Delta R I_{d.c.}$ generated during the precessional motion of the free-layer magnetization, we obtain for the narrowest peaks $\Delta U_{gen}^{OP} = 126\,\mu V$ ($I_{d.c.} = -1.1\,mA$ and $\Delta f = 139\,MHz$), which is more than twice as large as $\Delta U_{gen}^{IP} = 50\,\mu V$ ($I_{d.c.} = 1.2\,mA$ and $\Delta f = 50\,MHz$) for the IP mode. This confirms that OP precessions lead to a larger output signal. The presented 'perpendicular-polarizer/planar-free-layer/planar-analyser' spin-valve system thus validates for the first time the theoretical predictions for this configuration[18,26–28]. This will be of interest for the design of spin-torque oscillators with improved output signals and operated in zero external fields and at currents close to the threshold current I_c.

Note added in proof: In parallel to this work OP precessions have also been observed recently in non-conventional, 'wavy' planar spin valve nanopillars[39].

METHODS

SAMPLE FABRICATION

The continuous multilayer thin films were deposited in a Plassys sputtering system onto 100 mm high-resistivity ($\rho > 3\,k\Omega\,cm^2$) Si/SiO_2 substrates, that contain embedded bottom electrodes. The magnetic film composition is (in nanometres) Pol/Cu4/$Fe_{20}Ni_{80}$3/Co0.5/Cu3/Co3/$Ir_{20}Mn_{80}$5, with Pol=Pt20/$(Co0.55/Pt0.25)_5$/(Co0.8/Cu0.3/Co0.8) (B. Rodmacq *et al.* patent pending). From theoretical studies[35] it is predicted that Cu lamination of a Co layer results in a strong spin polarization over a very small thickness owing to additional interface scattering. With this the two interfaces in Co/Cu/Co correspond to an effective Co layer thickness of 20 nm (refs 35,36), which is one-half of the spin diffusion length of bulk Co ($l_{sf} = 38\,nm$). For a continuous film of Pol it has been checked by magnetometry measurements that the remanent magnetization is equal to the saturation magnetization. This indicates that the magnetization of the laminated Co layer on top of the Co/Pt multilayer is oriented OP.

The continuous film was patterned into nanopillars using conventional electron-beam lithography combined with reactive ion etching and ion beam etching techniques. After encapsulation by a SiO_2 oxide film, chemical mechanical polishing was used to open the top of the pillar to be contacted by the top electrode. The nanopillar is thus sandwiched between the bottom and top electrodes, which form impedance-matched coplanar waveguides. The entire nanofabrication process was carried out at CEA/LETI Grenoble.

TRANSPORT MEASUREMENTS

Transport measurements have been made by contacting the pillars via the top and bottom electrodes with high-bandwidth (40 GHz) probes. For the static measurements a standard Keithley Instruments sourcemeter was used. For the $R(I)$ loops in Fig. 4b (bottom), the $R(I)$ loop at $H_b = 0$ was subtracted to eliminate a parabolic background signal, which is due to sample heating. For the dynamic experiments[5], a bias T was used to separate the d.c. current injection from the dynamic output signal that was fed via a 40 dB low-noise amplifier into a 26 GHz spectrum analyser. The spectra in Fig. 5a were taken with a resolution bandwidth (RBW) of 1 MHz and show the power spectral density (PSD) of the output voltage ΔU, defined by $PSD = \Delta U(f)^2/RBW$. A baseline taken at $I_{d.c.} = 0\,mA$ was subtracted from the measured PSD data, and the amplifier gain was divided out.

The dynamic resistance variations ΔR_{IP} and ΔR_{OP}, plotted in Fig. 6, correspond to peak-to-peak values. They were obtained from the PSD by calculating the area under the respective peaks, yielding the total r.m.s. power ΔU^2. Furthermore, it has been considered that the nanopillar resistance R and the input impedance Z of the spectrum analyser form a voltage divider for the voltage ΔU_{gen} generated by the MR cell. With this, the dynamic peak-to-peak resistance variation ΔR is given by

$$\Delta R = 2\sqrt{2}\Delta R_{RMS} \quad \text{with} \quad \Delta R_{RMS} = \frac{\Delta U_{gen}}{I_{d.c.}}$$

$$\text{and} \quad \Delta U_{gen} = \left(\frac{Z+R}{Z}\right)\Delta U$$

where ΔR stands for ΔR_{IP} or ΔR_{OP}.

MACROSPIN SIMULATION

The zero-temperature macrospin simulations were carried out by solving the Landau–Lifschitz–Gilbert equation[23,24], enhanced by the Slonczewski spin-torque term, which was taken as[1] $STT = (\gamma a_j/\mu_0 M_s)\mathbf{M} \times (\mathbf{M} \times \mathbf{P})$ where γ is the gyromagnetic ratio and $a_j = (\hbar/2e)(I/M_s V)g(\eta)$. μ_0 is the vacuum permeability; $g(\eta)$ is the Slonczewski spin-polarization efficiency[1], which is a function of the current polarization η as well as the angle between the magnetization vector $\mathbf{M}$ and the spin-polarization direction $\mathbf{P}$. For simplicity, this angle has been taken constant at 90°. M_s and V are the free-layer saturation magnetization and volume respectively. The frequencies were obtained under the assumption that the trajectories can be approximated by constant-energy trajectories[25] (T. Valet, unpublished). The simulation parameters were $\mathbf{P} \parallel Z$, $M_s = 866\,kA\,m^{-1}$, $H_u = 8$ and $4\,kA\,m^{-1}$ as indicated in the figures, $\alpha = 0.02$ and $g = 0.17$ (corresponding to $\eta = 0.3$ close to the current polarization of Co (ref. 35)). The low values of the experimental frequencies suggest a damping constant α that is larger than the bulk value $\alpha = 0.01$, as has also been reported for other nanostructures[37,38]. The simulations in Fig. 2 were carried out using a perpendicular polarizer as described in ref. 30 by ignoring the spin-torque effect from the planar analyser. Details of calculations and results of the full structure will be addressed in a forthcoming publication.

Received 5 December 2006; accepted 5 April 2007; published 29 April 2007.

References

1. Slonczewski, J. C. Current-driven excitation of magnetic multilayers. *J. Magn. Magn. Mater.* **159**, L1–L7 (1996).
2. Slonczewski, J. C. Excitation of spin waves by an electric current. *J. Magn. Magn. Mater.* **195**, L261–L268 (1999).
3. Berger, L. Emission of spin waves by a magnetic multilayer traversed by a current. *Phys. Rev. B* **54**, 9353–9358 (1996).
4. Li, Z. & Zhang, S. Magnetization dynamics with a spin-transfer torque. *Phys. Rev. B* **68**, 24404–24413 (2003).
5. Kiselev, S. I. *et al.* Microwave oscillations of a nanomagnet driven by a spin-polarized current. *Nature* **425**, 380–383 (2003).
6. Kiselev, S. I. *et al.* Current-induced nanomagnet dynamics for magnetic fields perpendicular to the sample plane. *Phys. Rev. Lett.* **93**, 36601–36604 (2004).
7. Kiselev, S. I. *et al.* Spin-transfer excitations of permalloy nanopillars for large applied currents. *Phys. Rev. B* **72**, 64430–64439 (2005).
8. Rippard, W. H., Pufall, M. R., Kaka, S., Russek, S. E. & Silva, T. J. Direct-current induced dynamics in $Co_{90}Fe_{10}/Ni_{80}Fe_{20}$ point contacts. *Phys. Rev. Lett.* **92**, 27201–27204 (2004).
9. Rippard, W. H., Pufall, M. R., Kaka, S., Silva, T. J. & Russek, S. E. Current-driven microwave dynamics in magnetic point contacts as a function of applied field angle. *Phys. Rev. B* **70**, 100406–100409 (2004).
10. Krivorotov, I. N. *et al.* Time domain measurements of nanomagnet dynamics driven by spin-transfer torques. *Science* **307**, 228–231 (2005).
11. Kaka, S. *et al.* Mutual phase-locking of microwave spin torque nano-oscillators. *Nature* **437**, 389–392 (2005).

12. Mancoff, F. B., Rizzo, N. D., Engel, B. N. & Tehrani, S. Phase-locking in double-point-contact spin-transfer devices. *Nature* **437**, 393–395 (2005).
13. Rippard, W. H., Pufall, M. R., Kaka, S., Silva, T. J. & Russek, S. E. Injection locking and phase control of spin transfer oscillators. *Phys. Rev. Lett.* **95**, 67203–67206 (2005).
14. Pufall, M. R., Rippard, W. H., Russek, S. E., Kaka, S. & Katine, J. A. Electrical measurements of spin-wave interactions of proximate spin transfer nanooscillators. *Phys. Rev. Lett.* **97**, 87206–87209 (2006).
15. Mistral, Q. *et al*. Current-driven microwave oscillations in current perpendicular-to-plane spin-valve nanopillars. *Appl. Phys. Lett.* **88**, 192507–192509 (2006).
16. Valet, T. & Fert, A. Theory of the perpendicular magnetoresistance in magnetic multilayers. *Phys. Rev. B* **48**, 7099–7113 (1993).
17. Moodera, J. S. & Mathon, G. Spin polarized tunneling in ferromagnetic junctions. *J. Magn. Magn. Mater.* **200**, 248–273 (1999).
18. Slonczewski, J. C. Electronic device using magnetic components. US patent 5,695,864 (1997).
19. Apalkov, D. M. & Visscher, P. B. Spin-torque switching: Fokker–Planck rate calculation. *Phys. Rev. B* **72**, 180405–180408 (2005).
20. Slavin, A. N. & Tiberkevich, V. S. Nonlinear self-phase-locking effect in an array of current-driven magnetic nanocontacts. *Phys. Rev. B* **72**, 92407–92410 (2005).
21. Slavin, A. N. & Tiberkevich, V. S. Spinwave mode excited by spin-polarized current in a magnetic nanocontact is a standing self-localized wave bullet. *Phys. Rev. Lett.* **95**, 237201–237204 (2005).
22. Slavin, A. N. & Tiberkevich, V. S. Theory of mutual phaselocking of spin torque nano-oscillators preprint. *Phys. Rev. B* **74**, 10440–10443 (2006).
23. Slavin, A. N. & Tiberkevich, V. S. Current-induced bistability and dynamic range of microwave generation in magnetic nanostructures. *Phys. Rev. B* **72**, 94428–94432 (2005).
24. Stiles, M. D. & Miltat, J. in *Spin Dynamics in Confined Magntic Structures III* (eds Hillebrands, B. & Thiaville, A.) (Springer, Berlin, 2006).
25. Bertotti, G. *et al.* Magnetization switching and microwave oscillations in nanomagnets driven by spin-polarized currents. *Phys. Rev. Lett.* **94**, 127206–127209 (2005).
26. Redon, O., Dieny, B. & Rodmacq, B. Magnetic spin polarization and magnetization rotation device with memory and writing process using such a device. US patent 6,532,164 B2 (2003).
27. Lee, K. J., Redon, O. & Dieny, B. Analytical investigation of spin-transfer dynamics using a perpendicular-to-plane polarizer. *Appl. Phys. Lett.* **86**, 22505–22507 (2005).
28. Kent, A. D., Özyilmaz, B. & del Barco, E. Spin-transfer-induced precessional magnetization reversal. *Appl. Phys. Lett.* **84**, 3897–3899 (2004).
29. Mangin, S. *et al*. Current-induced magnetization reversal in nanopillars with perpendicular anisotropy. *Nature Mater.* **5**, 210–215 (2006).
30. Firastrau, I. *et al.* State diagram for the spin current induced magnetization dynamics using a perpendicular polarizer and a planar free layer. *J. Magn. Magn. Mater.* **31**, 2029–2031 (2007).
31. Katine, J. A., Albert, F. J., Buhrman, R. A., Myers, E. B. & Ralph, D. C. Current-driven magnetization reversal and spin-wave excitations in Co/Cu/Co pillars. *Phys. Rev. Lett.* **84**, 3149–3152 (2000).
32. Grollier, J. *et al*. Field dependence of magnetization reversal by spin transfer. *Phys. Rev. B* **67**, 174402–174409 (2003).
33. Lee, K. J., Deac, A., Redon, O., Nozieres, J. P. & Dieny, B. Excitations of incoherent spin-waves due to spin-transfer torque. *Nature Mater.* **3**, 877–881 (2004).
34. Seki, T., Mitani, S., Yakushiji, K. & Takanashi, K. Magnetization reversal by spin-transfer torque in 90° configuration with a perpendicular spin polarizer. *Appl. Phys. Lett.* **89**, 172504–172506 (2006).
35. Delille, F. *et al*. Thermal variation of current perpendicular-to-plane giant magnetoresistance in laminated and nonlaminated spin valves. *J. Appl. Phys.* **100**, 13912–13918 (2006).
36. Deac, A. *et al*. Current-induced magnetization switching in exchange-biased spin valves for current-perpendicular-to-plane giant magnetoresistance heads. *Phys. Rev. B* **73**, 64414–64421 (2006).
37. Krivorotov, I. N. *et al.* Time-domain measurements of nanomagnet dynamics driven by spin-transfer torques. *Science* **307**, 228–231 (2005).
38. Braganca, P. M. *et al*. Reducing the critical current for short-pulse spin-transfer switching of nanomagnets. *Appl. Phys. Lett.* **87**, 112507–112509 (2005).
39. Boulle, O. et al. Shaped angular dependence of the spin transfer torque and microwave generation without magnetic field. *Nature Phys.* (in the press).

Acknowledgements

This work has been supported by the French national programmes ANVAR No A0503013 and ANR/PNANO MagICO No ANR-05-NANO-044, as well as partially by the EC programme DYNAMICS No HPRN-CT-2002-00289. I.F. acknowledges support from the Institut Carnot funding of CEA/LETI. We thank A. Slavin, V. Tiberkevich and C. Baraduc for stimulating discussions, A. Manchon for simulations on the spin polarization and S. Petit for assistance with transport measurements.
Correspondence and requests for materials should be addressed to U.E.

Competing financial interests

The authors declare no competing financial interests.